

PHYSICS

Integrated Brillouin photonics in thin-film lithium niobate

Kaixuan Ye^{1†}, Hanke Feng^{2†}, Randy te Morsche¹, Chuangchuang Wei¹, Yvan Klaver¹, Akhileshwar Mishra¹, Zheng Zheng¹, Akshay Keloth¹, Ahmet Tarık Işık¹, Zhaoxi Chen², Cheng Wang^{2*}, David Marpaung^{1*}

Stimulated Brillouin scattering (SBS) is revolutionizing low-noise lasers and microwave photonics. However, a scalable and efficient integrated platform for Brillouin photonics has remained elusive. Here, we leverage the well-established thin-film lithium niobate (TFLN) platform to address these long-standing limitations. We report two distinct SBS processes on this platform, driven by surface acoustic wave (SAW) with 20-megahertz linewidth or bulk acoustic waves with a linewidth 200 times broader. Exploiting the strong SAW SBS gain, we demonstrate a narrowband internal net gain amplifier overcoming propagation losses. In addition, we achieve a stimulated Brillouin laser in TFLN, featuring a tuning range exceeding 20 nanometers and enabling high-purity radio frequency signal generation with an intrinsic linewidth of 9 hertz. Furthermore, we develop a programmable, multifunctional integrated Brillouin microwave photonic processor capable of notch filtering, bandpass filtering, or true time delay. This work bridges SBS with advanced TFLN technologies such as high-speed modulators and wide-band optical frequency combs, unlocking new paradigms for integrated Brillouin photonics.

INTRODUCTION

Stimulated Brillouin scattering (SBS), arising from the coherent optomechanical interaction between photons and phonons, is transforming integrated photonics (1). With its narrowband gain window, SBS is essential for high-selectivity filters (2–4) and amplifiers (5) in the next-generation optical and radio communications systems (6). Its unique acoustic dissipation mechanism enables subhertz linewidth integrated lasers (7, 8) and high-purity radio frequency (RF) signal generators (9–11). Furthermore, manipulating its phase matching condition gives rise to on-chip nonreciprocal devices (12, 13).

Nevertheless, finding a versatile and scalable photonics platform that supports SBS remains a significant challenge. Achieving strong on-chip SBS gain requires large photoelastic coefficients, simultaneous guidance of both the optical and acoustic waves, and low propagation loss. While proof-of-concept applications have been demonstrated across various material platforms—including chalcogenide (14–16), silicon (5, 17–20), silicon nitride (7, 21–24), and aluminum nitride (25)—these platforms face critical challenges that hinder scalability and practical deployment. For instance, chalcogenide (As₂S₃) waveguides suffer from photosensitivity and thermal instability at high power (26), limiting their long-term reliability. Silicon nitride waveguides, despite their low propagation loss, exhibit an SBS gain more than two orders of magnitude lower than chalcogenide, making them insufficient for most microwave photonic (MWP) applications (21). Meanwhile, Brillouin-active suspended silicon waveguides present significant fabrication challenges and structural instability (5, 18), restricting their viability for large-scale integration.

Harnessing SBS in the thin-film lithium niobate (TFLN) platform can elevate the SBS technology to a new level of readiness. Renowned

for its exceptional scalability, low optical losses, and significant electro-optic (EO) coefficients (27, 28), TFLN has unlocked a variety of novel applications with exceptional performances, including on-chip EO modulators (29), optical frequency combs (30, 31), MWP processors (32), and integrated lasers (33, 34). Expanding the capabilities of TFLN to include SBS not only enables Brillouin-based applications on a more scalable platform, but also creates a synergistic interplay with its existing functionalities. While optomechanical effects in TFLN have been explored using electric interdigital transducers (35–39), the investigation of SBS in this platform remains in its infancy (40–42), with no Brillouin-based applications yet reported.

Here, we observe and utilize SBS process in the TFLN platform for system-level applications. Two distinct SBS processes are identified: one driven by surface acoustic wave (SAW) with 20-MHz linewidth and the other by bulk acoustic waves with a broader linewidth exceeding 4 GHz in a circular spiral geometry. The high SAW SBS gain unlocks a versatile Brillouin photonics engine with multiple functionalities in TFLN. First, we demonstrate an internal net gain amplifier that surpasses intrinsic propagation losses within a 10-cm spiral waveguide. Second, by incorporating SBS gain into a high-quality racetrack resonator, we generate a stimulated Brillouin laser (SBL) in TFLN, achieving a tuning range greater than 20 nm and supporting high-purity RF signal generation with an intrinsic linewidth of 9 Hz. Last, we develop a versatile Brillouin-based MWP processor supporting programmable functionalities including notch filtering, bandpass filtering, and true time delay, with SBS spirals, on-chip modulators, and cascaded tunable rings all implemented on a single platform.

RESULTS

TFLN Brillouin photonics engine

Figure 1A illustrates an envisioned monolithic TFLN Brillouin photonic circuit. The cladded region incorporates high performance building blocks traditionally demonstrated in TFLN, including an efficient on-chip EO modulator for high-speed microwave-to-optical

¹Nonlinear Nanophotonics Group, MESA+ Institute of Nanotechnology, University of Twente, Enschede, Netherlands. ²Department of Electrical Engineering and State Key Laboratory of Terahertz and Millimeter Waves, City University of Hong Kong, Hong Kong, China.

*Corresponding author. Email: cwang257@cityu.edu.hk (C.Wa.); david.marpaung@utwente.nl (D.M.)

†These authors contributed equally to this work.

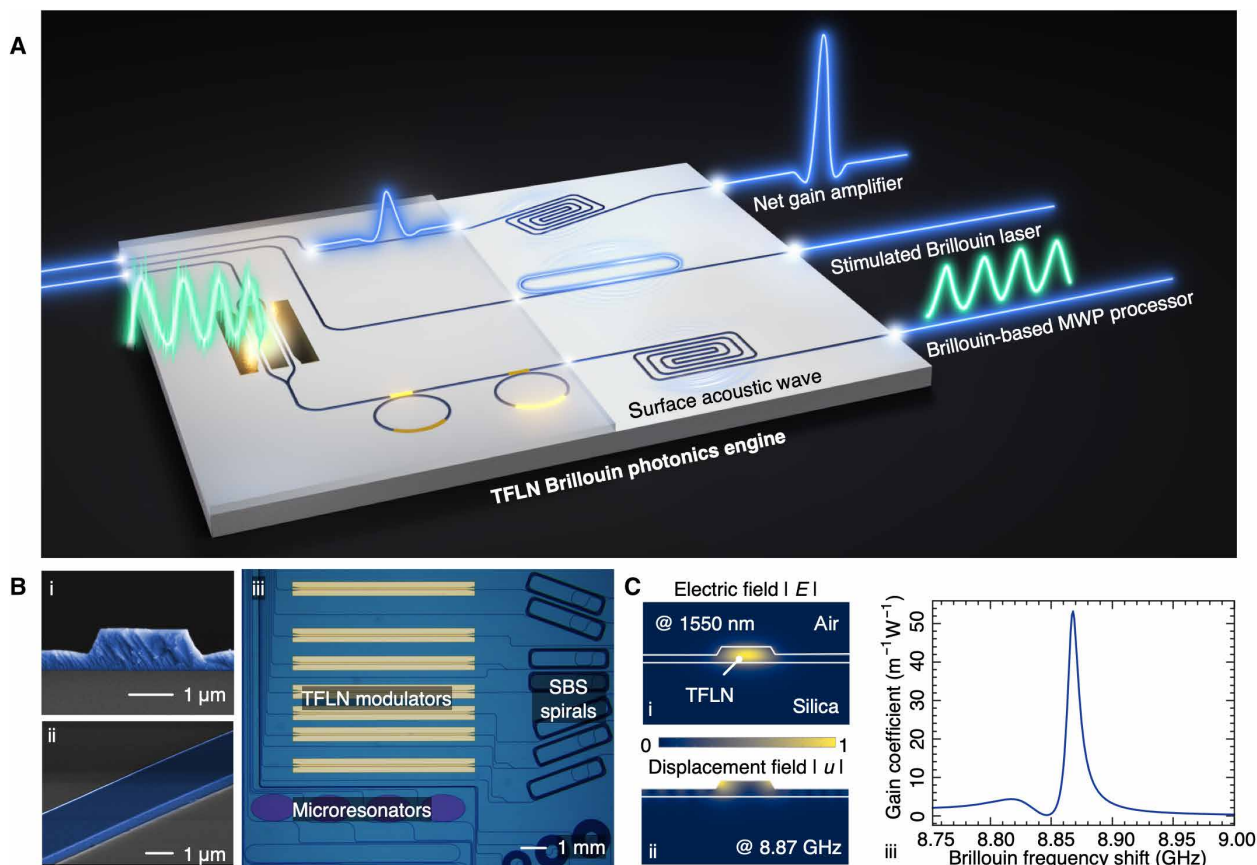


Fig. 1. Monolithic TFLN Brillouin photonics engine. (A) Illustration of a TFLN circuit that contains high-speed electro-optic modulators, tunable rings, and SBS-active devices, enabling net gain amplifier, stimulated Brillouin laser, and Brillouin-based microwave photonics processor. (B) (i) Scanning electron microscope (SEM) image of the cross section of the half-etched TFLN waveguide; (ii) SEM image of the TFLN waveguide sidewall, showing small roughness; and (iii) microscope image of a TFLN sample that integrates modulators, spirals, and resonators together. (C) Simulated SBS responses of an x-cut 0° TFLN waveguide, with the electric field, displacement field, and the gain coefficient profile shown in (i) to (iii), respectively.

wave conversion and low-loss tunable ring resonators for programmable signal processing. Meanwhile, monolithic integration with the uncladded region unlocks new SBS functions in this platform, including narrow-bandwidth RF signal processing, high-purity RF signal generation via the Brillouin laser, and highly selective optical amplification.

Our TFLN circuits are fabricated with a wafer-scale ultraviolet (UV) stepper lithography system (see Materials and Methods). The waveguides are half-etched with a width of $1.5\ \mu\text{m}$ (Fig. 1B, i and ii), optimized to achieve a balance between tight optical mode confinement and low propagation loss. This standard waveguide structure supports the monolithic integration of high-speed TFLN modulators, centimeter-long SBS-active spirals, and high-quality factor resonators on a single chip (Fig. 1B, iii). Furthermore, the uncladded structure enables strong overlap of SAW with the optical mode, leading to significant SBS gain in this platform (Fig. 1C).

Angle-dependent strong SBS in TFLN

We achieve strong SBS gain in both z-cut and x-cut uncladded TFLN waveguides by leveraging the intrinsic anisotropy of lithium niobate (40). The Brillouin gain coefficient, a critical parameter quantifying the SBS strength, is determined by the photoelastic coefficients and the optoacoustic overlap that requires acoustic wave

confinement. Both parameters can be significantly tailored through varying the rotational angle of the waveguides with respect to the crystalline orientation of the wafer (43).

In particular, we obtained large optoacoustic overlap with SAW that is confined in the TFLN waveguide at specific rotational angles. At these angles, SAW propagates slower than acoustic waves in the silica undercladding, preventing acoustic leakages that plagued the propagation of bulk acoustic waves in these waveguides.

We validated the significant Brillouin gain coefficients and the angle-dependent SBS responses in TFLN using z-cut waveguides with varying rotational angles (Fig. 2A). The Brillouin gain coefficient reaches $84.9\ \text{m}^{-1}\text{W}^{-1}$ in the 20° waveguide (see the Supplementary Materials for experimental details), representing a more than 200-fold enhancement compared to the standard low-loss silicon nitride platforms (7, 21, 22). This gain coefficient decreases to $25.6\ \text{m}^{-1}\text{W}^{-1}$ in the 40° waveguide and further drops to $9.4\ \text{m}^{-1}\text{W}^{-1}$ in the 0° one. Meanwhile, the Brillouin frequency shift changes from 8.36 GHz in the 0° waveguide to 8.14 GHz in the 20° waveguide and 7.92 GHz in the 40° waveguide (Fig. 2B). A comprehensive comparison with other state-of-the-art Brillouin active integrated platforms is provided in the Supplementary Materials.

Equally strong SBS gain can also be observed in x-cut TFLN waveguides, of which most high-speed, low- $V\pi$, on-chip modulators

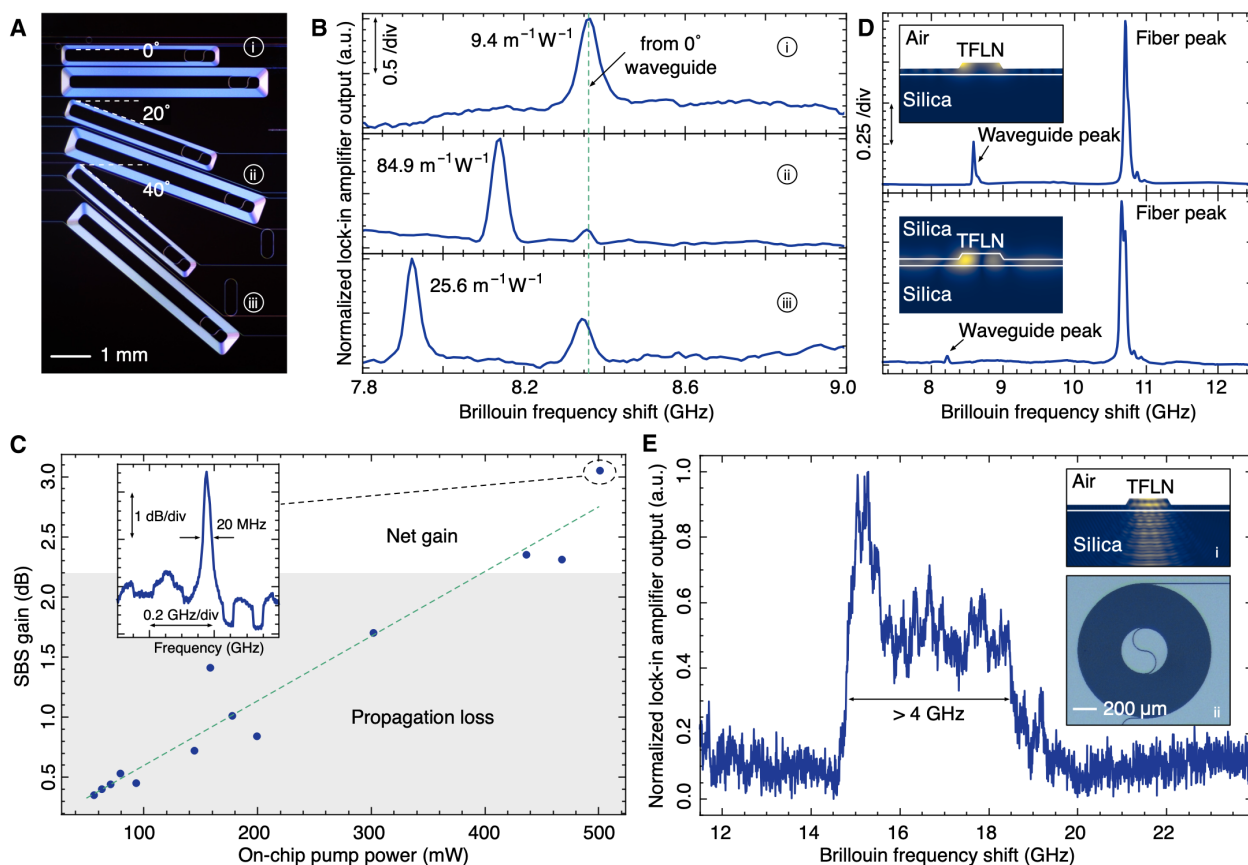


Fig. 2. Angle-dependent strong SBS responses in the TFLN platform. (A) Microscope image of a z-cut TFLN sample that contains waveguides with a rotational angle of 0° , 20° , and 40° . (B) SBS responses of z-cut TFLN waveguides measured with a lock-in amplifier based setup. The prominent peaks at 8.3 GHz in all three panels correspond to the 0° waveguide, while additional peaks in (ii) and (iii) arise from waveguides at 20° and 40° , respectively, as labeled in (A). (C) Measured SBS gain as a function of on-chip pump power. Net internal gain amplification is achieved when the pump power exceeds 400 mW. Inset: SBS response from a 10-cm-long x-cut 0° TFLN waveguide, showing SBS gain exceeding 3 dB, which overcomes intrinsic propagation losses. (D) Comparison of SBS responses in uncladded and cladded x-cut TFLN waveguides. The stronger SBS response in the uncladded sample validates the role of SAW in enhancing the SBS responses in TFLN. Insets: Simulated displacement fields of the acoustic waves, illustrating better confinement in the air-cladded structure. (E) Measured SBS response from an 8-cm-long circular spiral, demonstrating a bandwidth exceeding 4 GHz. Insets: (i) Simulated displacement field of the bulk acoustic wave driving this SBS process. (ii) Microscope image of the 8-cm-long circular spiral.

are made. Harnessing SBS in the x-cut TFLN platform enables full compatibility between SBS and on-chip modulators for Brillouin MWP applications. We achieve internal net gain amplification from a 10-cm-long x-cut 0° spiral waveguide with a Brillouin gain coefficient of $29.3 \text{ m}^{-1} \text{ W}^{-1}$. The SBS gain reaches 3 dB at a pump power of 500 mW, overcoming the 2.2-dB intrinsic propagation loss (Fig. 2C). Currently, the measured SBS gain is limited by the high coupling loss, the instability of the lensed fiber at high pump power, and the power-handling constraints of the fiber components in the setup. Nevertheless, off-chip net gain is achievable with optimized coupler design (44), which could reduce the coupling loss from current 7 dB per facet to 1 dB per facet. Increasing the spiral length and reducing waveguide propagation loss could further enhance the net SBS gain, positioning it as a unique narrowband amplifier for optical and radio communications.

The role of SAW in enhancing SBS gain is experimentally verified by comparing waveguides with and without a top silica cladding. Specifically, the Brillouin gain coefficient in the x-cut 0° uncladded waveguide is four times higher than the $7.0 \text{ m}^{-1} \text{ W}^{-1}$ observed in the

cladded waveguide, where SAW is suppressed. Simulated displacement fields shown in Fig. 2D further illustrate the improved acoustic confinement enabled by the SAW.

Spectral control of SBS response holds immense potential in realizing tunable optical and microwave filters (45). Traditionally, this has been achieved through multipump (45, 46) or strain tailoring (47, 48). Here, we show shaping of ultrabroadband SBS response through interaction with bulk acoustic waves in a circular spiral waveguide and enable 200 times broader linewidth (up to 4 GHz, Fig. 2E) than that of the SAW SBS process on the same platform (see the Supplementary Materials for more details). The coexistence of two SBS processes with distinct linewidths set it apart from other SAW SBS platforms (15, 23, 49). By selectively interacting with surface or bulk acoustic waves and leveraging the anisotropic SBS response, the TFLN platform enables a lithographically controlled approach to tailoring the SBS linewidth for specific Brillouin-based applications, including switchable Brillouin sources for photon/phonon linewidth narrowing and flat-top filters with sharp roll-offs at the transition bands.

Stimulated Brillouin lasers

Incorporating SBS gain within a high-quality factor resonator enables SBL generation in the TFLN platform. The SBL is generated in a 0° x-cut TFLN racetrack resonator, with the setup illustrated in Fig. 3A. The resonator features a high intrinsic quality factor of 1.78 million (Fig. 3B) and a free spectral range (FSR) of 8.57 GHz that aligns well with the Brillouin frequency shift of the 0° x-cut TFLN waveguide. By tuning

pump laser into the resonance of the racetrack resonator, we observed counterpropagating SBL signal with a frequency down-shifted by one FSR (Fig. 3C). Under different pump-to-resonance detuning frequencies (see the Supplementary Materials for more experimental details), we also observed four-wave mixing (FWM) of the light (Fig. 3D) and the coexistence of the FWM and SBL signals (Fig. 3E). The variations in the nonlinear dynamics observed in Fig. 3 (C to E) arise from the

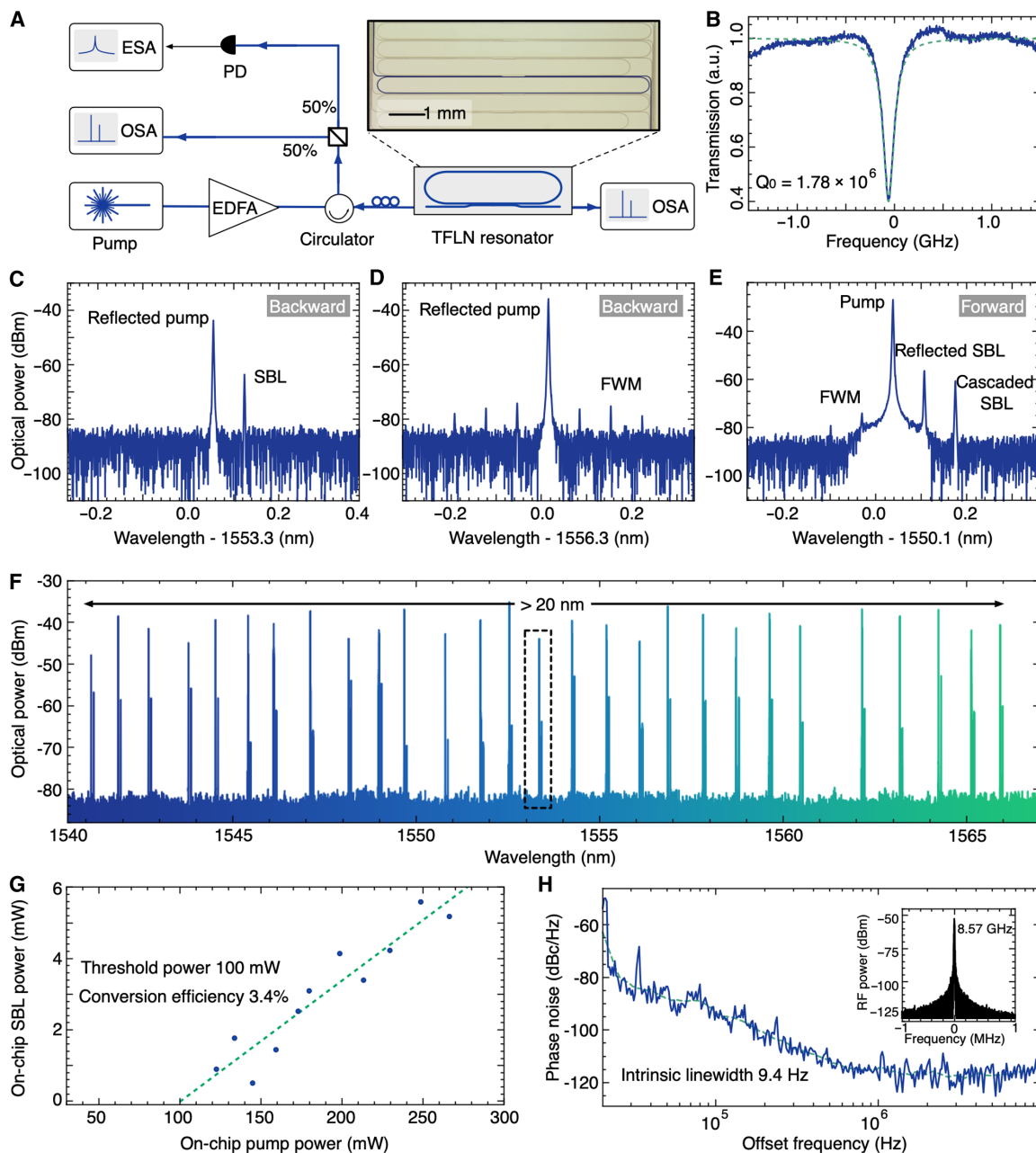


Fig. 3. SBL demonstration in a TFLN racetrack resonator. (A) Experimental setup of the SBL demonstration. EDFA, erbium-doped fiber amplifier; OSA, optical spectrum analyzer; ESA, electrical spectrum analyzer. (B) Measured optical transmission spectrum of the racetrack resonator, with an intrinsic quality factor of 1.78 million. (C) Optical spectrum of the observed SBL at 1553.35 nm. (D) Optical spectrum of the observed four-wave mixing (FWM) of the light from the TFLN resonator at 1556.32 nm. (E) Optical spectrum of the Brillouin-Kerr interaction at 1550.14 nm. Plots in (C) to (E) are with different pump to resonance detuning frequencies. (F) Widely tunable SBL from 1540 to 1567 nm, with the tuning range only constrained by EDFA gain bandwidth. Dashed rectangle corresponds to the zoomed-in spectrum shown in (C). (G) Measured on-chip SBL power versus the on-chip pump power. The linear fitting gives a threshold power of 100 mW and a pump-to-SBL conversion efficiency of 3.4%. (H) Measured single-sideband phase noise of the generated RF signal from the beating of the SBL and the pump. The extracted intrinsic linewidth of this signal is 9.4 Hz. Inset: measured RF spectrum, resolution bandwidth: 51 Hz.

interplay between SBS and Kerr nonlinearities, as well as possible external factors such as coupling stability, temperature fluctuations, and the pyroelectric effect of lithium niobate. While Brillouin-Kerr interactions have been studied in silica microdisk for soliton generation (50), a rigorous theoretical analysis of these nonlinear interactions in TFLN, along with the influence of other nonlinear effects, requires more comprehensive modeling. When the pump power is below the SBL threshold power, we also observed the Brillouin-induced transparency (12) (see the Supplementary Materials for details).

The ultralow dispersion of TFLN waveguides enables a wide wavelength tuning range of the SBL. The calculated group velocity dispersion (β_2) of the resonator is as low as $223 \text{ ps}^2/\text{km}$ ($D_2/2\pi = -13.6 \text{ kHz}$), ensuring that the FSR closely aligns with the Brillouin frequency shift across a wide wavelength range. As a result, the SBL can be tuned from 1540 to 1567 nm (Fig. 3F), with the tuning range primarily limited by the operational bandwidth of the applied erbium-doped fiber amplifier (EDFA).

We further characterized the threshold power and the conversion efficiency of the SBL (Fig. 3G). By varying the on-chip pump power from 120 to 270 mW, we estimated a threshold power of 100 mW and a conversion efficiency of 3.4%. To further reduce the threshold power, the coupling coefficient from the bus waveguide to the resonator can be increased to near-critical coupling. Moreover, a coupled ring molecule can be applied to reduce the mode volume, which also leads to a lower threshold power (24).

The SBL in the TFLN platform holds great promise for high-purity RF signal generation. Unlike prior demonstrations in silicon nitride (7), chalcogenide (8), and bulk lithium niobate (51), where the SBS linewidth exceeds the optical cavity linewidth, the 20-MHz SBS linewidth in the 0° x-cut TFLN waveguide is narrower than the linewidth of the racetrack resonator. Rather than optical linewidth narrowing, this unique regime of Brillouin lasing enables phonon linewidth narrowing (11), leading to the generation of a pure RF signal from the beating note between the pump and the SBL. We measured the single-sideband phase noise of the RF signal and extracted an intrinsic linewidth of 9.4 Hz (Fig. 3H). This positions the SBL in the TFLN platform as a promising candidate for compact, low-noise RF oscillators (9, 10).

In the future, technical noise at lower frequencies can be mitigated with laser stabilization techniques, such as using an optical reference cavity (52), or a Pound-Drever-Hall (PDH) lock circuit (53). For applications requiring ultralow optical linewidth, the TFLN SBL can also be driven by the bulk acoustic wave SBS process, where the SBS linewidth is broader than the resonance linewidth of the resonator.

Multifunctional integrated Brillouin MWP processor

We combine the SBS gain with the versatile device toolbox available on the TFLN platform to realize a high-performance multifunctional integrated Brillouin MWP processor. Specifically, high-speed EO modulators convert broadband microwave signals into optical domain. Cascaded tunable microrings fabricated on the same chip can be tuned to transform the intensity-modulated signal to various modulation formats, including phase modulation, single sideband modulation, and asymmetric dual-sideband modulation (2). At the same time, the SBS gain provided by the spiral waveguide enables ultra-narrowband selective processing of the sidebands. Diverse signal processing functionalities can be achieved after converting the dynamically programmed signal back to the microwave domain (Fig. 4A).

Figure 4 (B to E) showcases various MWP functionalities achieved by connecting a programmable MWP circuit—comprising an intensity modulator and four cascaded tunable rings (54)—to a 10-cm-long 0° x-cut spiral waveguide. By applying the frequency response of an over-coupled ring to the upper sideband of the intensity-modulated signal and compensating the amplitude at specific frequencies with the SBS gain, a notch filter with a high rejection ratio is demonstrated (Fig. 4B). Furthermore, the intensity modulation is transformed into phase modulation by exploiting the phase response of the over-coupled ring. Selective amplification of the upper sideband via the SBS gain results in a bandpass filter with 13 dB extinction ratio (Fig. 4C) or a notch filter with 25 MHz bandwidth and a rejection ratio larger than 47 dB (Fig. 4D). The link gain of this notch filter at the pass band is -40 dB , which can be further improved with lower coupling loss and higher optical power at the photodiode. In addition, placing two closely spaced critically coupled rings at the lower sideband allows for the conversion of intensity modulation into single-sideband modulation within a specific frequency range. Applying the SBS gain at the corresponding upper sideband enables the demonstration of RF true time delay larger than 4 ns (Fig. 4E) (see the Supplementary Materials for further experimental details).

This demonstration presents a Brillouin-based MWP processor that integrates SBS-active waveguides, modulators, and tunable rings within the same platform. Future optimizations could enable monolithic integration of all these building blocks on a single chip, further enhancing link gain and improving noise performance.

DISCUSSION

In this work, we harness strong SBS in the TFLN platform by exploiting the anisotropy of the material. The significant SBS gain makes TFLN an ideal platform for developing a Brillouin photonics engine capable of diverse functionalities. As proof-of-concept demonstrations, we realized net-gain Brillouin amplifiers, generated the SBL, and devised a multifunctional Brillouin-based MWP processor, all within the standard TFLN platform.

To further enhance performance, coupling loss between fiber and waveguide could potentially be reduced from 7 dB per facet to less than 1 dB per facet with dedicated spot-size converters (44). In addition, antiresonance waveguide structure could be applied to further enhance the SBS gain through improved acoustic confinement (17). Moreover, incorporating a coupled ring molecule design would allow for Brillouin laser generation with reduced threshold power, improved conversion efficiency, and a smaller device footprint.

Embedding this Brillouin photonics engine in a large-scale TFLN circuit could open the door to novel applications with unprecedented performances. For instance, the narrow SBS linewidth can be exploited to demonstrate a compact, high-resolution Brillouin optical spectrum analyzer (55). In RF photonic systems, integrating the SBS spiral with high-speed TFLN modulators and tunable rings on a single chip could increase the link gain and lower the noise figure (54). Furthermore, the Brillouin-Kerr interaction in TFLN could lead to on-chip Brillouin-Kerr combs (50).

MATERIALS AND METHODS

The TFLN samples under test are fabricated with lithium niobate on insulator (LNOI) wafers from NANOLN. The lithium niobate film is 500 nm thick in the x-cut LNOI wafer and 400 nm thick in the z-cut

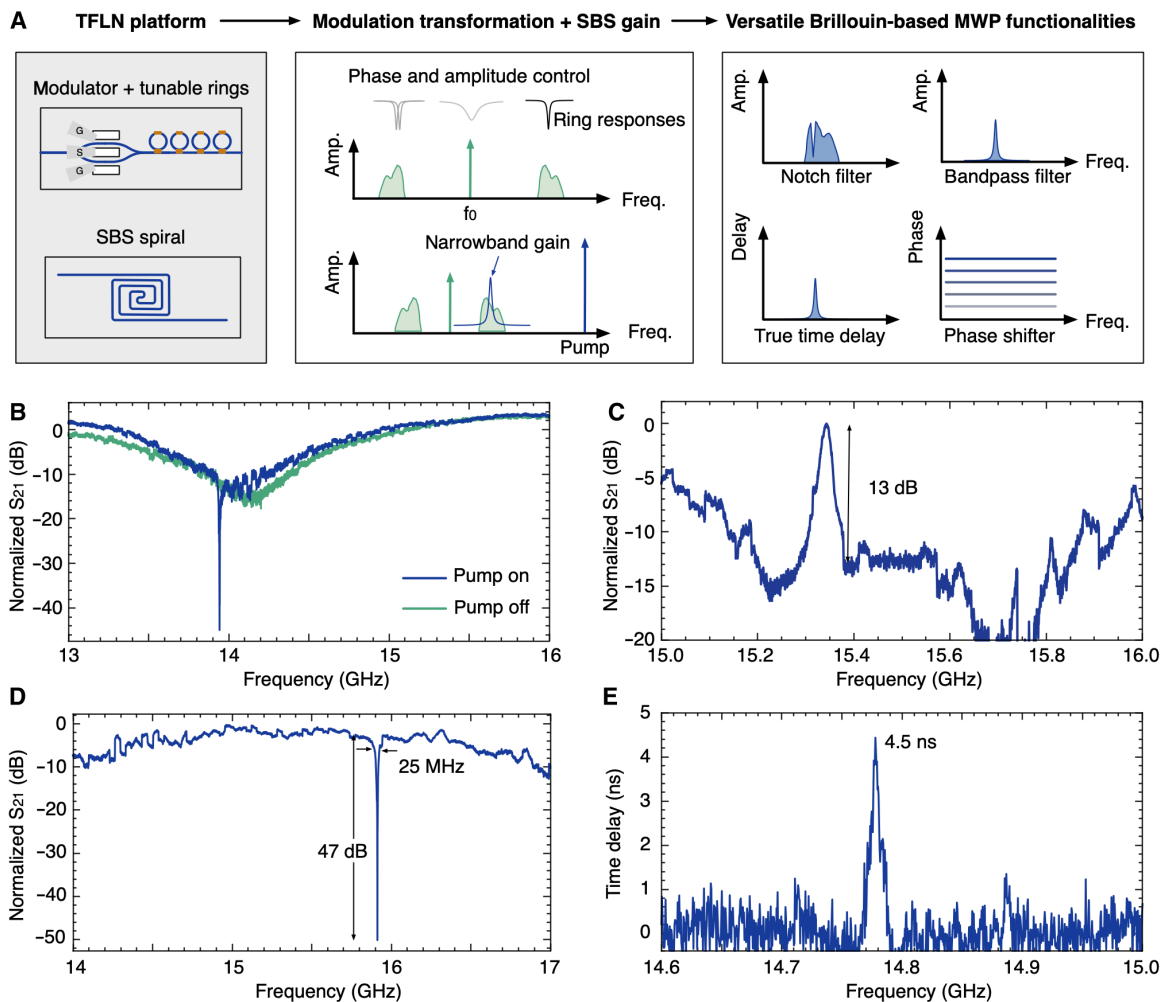


Fig. 4. Multifunctional integrated Brillouin MWP processor. (A) Schematic concept of the multifunctional integrated Brillouin MWP processor on the TFLN platform. The TFLN platform can host high-speed on-chip modulators, tunable rings, and SBS spirals. The tunable rings flexibly control the phase and amplitude of the modulated signal, enabling the transformation of intensity modulation into various modulation formats. Meanwhile, the SBS process introduces selective gain and phase shifts to the sidebands for signal processing. Upon conversion back into the microwave domain, this processor enables a wide range of MWP functionalities. (B) Measured notch filter responses achieved by imposing an over-coupled ring response on the sideband. (C) Measured response of Brillouin-based bandpass filter. (D) An alternative notch filter achieved by exploiting the asymmetric phase modulation with the SBS gain. (E) Demonstration of the RF true time delay.

LNOI wafer. First, SiO_2 is deposited on the surface of a 4-inch (100-mm) LNOI wafer as an etching hard mask using plasma-enhanced chemical vapor deposition PECVD. Waveguides are patterned with a UV stepper with a resolution of 500 nm. Afterward, the patterns are transferred to the SiO_2 layer with a fluorine-based dry etching process and then to the lithium niobate layer with an optimized Ar^+ -based inductively coupled plasma ICP reactive-ion etching process. The lithium niobate is half-etched, leaving a 250-nm-thick slab in the x-cut wafer and 200 nm in the z-cut one. The wafer is annealed after the removal of the SiO_2 mask.

Supplementary Materials

This PDF file includes:

Supplementary Text
Figs. S1 to S16
Tables S1 to S4

REFERENCES AND NOTES

- B. J. Eggleton, C. G. Poulton, P. T. Rakich, M. J. Steel, G. Bahl, Brillouin integrated photonics. *Nat. Photonics* **13**, 664–677 (2019).
- D. Marpaung, B. Morrison, M. Pagani, R. Pant, D.-Y. Choi, B. Luther-Davies, S. J. Madden, B. J. Eggleton, Low-power, chip-based stimulated Brillouin scattering microwave photonic filter with ultrahigh selectivity. *Optica* **2**, 76–83 (2015).
- M. Garrett, Y. Liu, M. Merklein, C. T. Bui, C. K. Lai, D. Y. Choi, S. J. Madden, A. Casas-Bedoya, B. J. Eggleton, Integrated microwave photonic notch filter using a heterogeneously integrated Brillouin and active-silicon photonic circuit. *Nat. Commun.* **14**, 7544 (2023).
- W. Xu, M. Zerbib, A. Iyer, J.-C. Beugnot, W. H. Renninger, Tunable Brillouin-based microwave photonic bandpass filter with sub-MHz bandwidth, in *CLEO* (Optica Publishing Group, 2024), p. FTh1D.5.
- E. A. Kittlaus, H. Shin, P. T. Rakich, Large Brillouin amplification in silicon. *Nat. Photonics* **10**, 463–467 (2016).
- D. Marpaung, J. Yao, J. Capmany, Integrated microwave photonics. *Nat Photonics* **13**, 80–90 (2019).
- S. Gundavarapu, G. M. Brodnik, M. Puckett, T. Huffman, D. Bose, R. Behunin, J. Wu, T. Qiu, C. Pinho, N. Chauhan, J. Nohava, P. T. Rakich, K. D. Nelson, M. Salit, D. J. Blumenthal, Sub-hertz fundamental linewidth photonic integrated Brillouin laser. *Nat. Photonics* **13**, 60–67 (2019).

8. K. Ko, D. Suk, D. Kim, S. Park, B. Sen, D.-G. Kim, Y. Wang, S. Dai, X. Wang, R. Wang, B. J. Chun, K.-H. Ko, P. T. Rakich, D.-Y. Choi, H. Lee, A mid-infrared Brillouin laser using ultra-high-Q on-chip resonators. *arXiv: 2404.06764 [physics.optics]* (2024).
9. W. Loh, D. Gray, R. Irion, O. May, C. Belanger, J. Plant, P. W. Juodawlkis, S. Yegnanarayanan, Ultralow noise microwave synthesis via difference frequency division of a Brillouin resonator. *Optica* **11**, 492–497 (2024).
10. B. M. Heffernan, J. Greenberg, T. Hori, T. Tanigawa, A. Rolland, Brillouin laser-driven terahertz oscillator up to 3 THz with femtosecond-level timing jitter. *Nat. Photonics* **18**, 1263–1268 (2024).
11. N. T. Otterstrom, R. O. Behunin, E. A. Kittlaus, Z. Wang, P. T. Rakich, A silicon Brillouin laser. *Science* **360**, 1113–1116 (2018).
12. J. Kim, M. C. Kuzyk, K. Han, H. Wang, G. Bahl, Non-reciprocal Brillouin scattering induced transparency. *Nat. Phys.* **11**, 275–280 (2015).
13. Y. Zhou, F. Ruesink, S. Gertler, H. Cheng, M. Pavlovich, E. Kittlaus, A. L. Starbuck, A. J. Leenheer, A. T. Pomerene, D. C. Trotter, C. Dallo, K. M. Musick, E. Garcia, R. Reyna, A. L. Holterhoff, M. Gehl, A. Kodigala, J. Bowers, M. Eichenfield, N. T. Otterstrom, A. L. Lentine, P. Rakich, Nonreciprocal dissipation engineering via strong coupling with a continuum of modes. *Phys. Rev. X* **14**, 021002 (2024).
14. R. Pant, C. G. Poulton, D.-Y. Choi, H. Mcfarlane, S. Hile, E. Li, L. Thevenaz, B. Luther-Davies, S. J. Madden, B. J. Eggleton, On-chip stimulated Brillouin scattering. *Opt. Express* **19**, 8285–8290 (2011).
15. G. Neijts, C. K. Lai, M. K. Riseng, D.-Y. Choi, K. Yan, D. Marpaung, S. J. Madden, B. J. Eggleton, M. Merklein, On-chip stimulated Brillouin scattering via surface acoustic waves. *APL Photonics* **9**, 106114 (2024).
16. B. Morrison, A. Casas-Bedoya, G. Ren, K. Vu, Y. Liu, A. Zarifi, T. G. Nguyen, D.-Y. Choi, D. Marpaung, S. Madden, A. Mitchell, B. J. Eggleton, Compact Brillouin devices through hybrid integration on silicon. *Optica* **4**, 847–854 (2017).
17. P. Lei, M. Xu, Y. Bai, Z. Chen, X. Xie, Anti-resonant acoustic waveguides enabled tailorable Brillouin scattering on chip. *Nat. Commun.* **15**, 3877 (2024).
18. R. Van Laer, B. Kuyken, D. Van Thourhout, R. Baets, Interaction between light and highly confined hypersound in a silicon photonic nanowire. *Nat. Photonics* **9**, 199–203 (2015).
19. T. Dinter, M. K. Schmidt, M. J. Steel, Anti-resonant reflecting acoustic rib waveguides for strong opto-acoustic interaction. *arXiv: 2409.14756 [physics.optics]* (2024).
20. D. Munk, M. Katzman, M. Hen, M. Priel, M. Feldberg, T. Sharabani, S. Levy, A. Bergman, A. Zadok, Surface acoustic wave photonic devices in silicon on insulator. *Nat. Commun.* **10**, 4214 (2019).
21. F. Gyger, J. Liu, F. Yang, J. He, A. S. Raja, R. N. Wang, S. A. Bhave, T. J. Kippenberg, L. Thevenaz, Observation of stimulated Brillouin scattering in silicon nitride integrated waveguides. *Phys. Rev. Lett.* **124**, 013902 (2020).
22. R. Botter, K. Ye, Y. Klaver, R. Suryadharma, O. Daulay, G. Liu, J. van den Hoogen, L. Kanger, P. van der Slot, E. Klein, M. Hoekman, C. Roeloffzen, Y. Liu, D. Marpaung, Guided-acoustic stimulated Brillouin scattering in silicon nitride photonic circuits. *Sci. Adv.* **8**, eabq2196 (2022).
23. Y. Klaver, R. te Morsche, R. A. Botter, B. Hashemi, B. L. S. Frare, A. Mishra, K. Ye, H. Mbonde, P. T. Ahmadi, N. M. Taleghani, E. Jonker, R. B. G. Braamhaar, P. R. Selvaganapathy, P. Mascher, P. J. M. van der Slot, J. D. B. Bradley, D. Marpaung, Surface acoustic waves Brillouin photonics on a silicon nitride chip. *arXiv: 2410.16263 [physics.optics]* (2024).
24. Q.-X. Ji, P. Liu, W. Jin, J. Guo, L. Wu, Z. Yuan, J. Peters, A. Feshali, M. Paniccia, J. E. Bowers, K. J. Vahala, Multimodality integrated microresonators using the Moiré speedup effect. *Science* **383**, 1080–1083 (2024).
25. Q. Liu, H. Li, M. Li, Electromechanical Brillouin scattering in integrated optomechanical waveguides. *Optica* **6**, 778–785 (2019).
26. D. Xia, Z. Yang, P. Zeng, B. Zhang, J. Wu, Z. Wang, J. Zhao, J. Huang, L. Luo, D. Liu, S. Yang, H. Guo, Z. Li, Integrated chalcogenide photonics for microresonator soliton combs. *Laser Photon. Rev.* **17**, 2200219 (2023).
27. A. Boes, L. Chang, C. Langrock, M. Yu, M. Zhang, Q. Lin, M. Lončar, M. Fejer, J. Bowers, A. Mitchell, Lithium niobate photonics: Unlocking the electromagnetic spectrum. *Science* **379**, eabj4396 (2023).
28. D. Zhu, L. Shao, M. Yu, R. Cheng, B. Desiatov, C. J. Xin, Y. Hu, J. Holzgrafe, S. Ghosh, A. Shams-Ansari, E. Puma, N. Sinclair, N. Sinclair, C. Reimer, M. Zhang, M. Lončar, Integrated photonics on thin-film lithium niobate. *Adv. Opt. Photonics* **13**, 242–352 (2021).
29. C. Wang, M. Zhang, X. Chen, M. Bertrand, A. Shams-Ansari, S. Chandrasekhar, P. Winzer, M. Lončar, Integrated lithium niobate electro-optic modulators operating at CMOS-compatible voltages. *Nature* **562**, 101–104 (2018).
30. M. Zhang, B. Buscaino, C. Wang, A. Shams-Ansari, C. Reimer, R. Zhu, J. M. Kahn, M. Lončar, Broadband electro-optic frequency comb generation in a lithium niobate microring resonator. *Nature* **568**, 373–377 (2019).
31. T.-H. Wu, L. Ledezma, C. Fredrick, P. Sekhar, R. Sekine, Q. Guo, R. M. Briggs, A. Marandi, S. A. Diddams, Visible-to-ultraviolet frequency comb generation in lithium niobate nanophotonic waveguides. *Nat. Photonics* **18**, 218–223 (2024).
32. H. Feng, T. Ge, X. Guo, B. Wang, Y. Zhang, Z. Chen, S. Zhu, K. Zhang, W. Sun, C. Huang, Y. Yuan, C. Wang, Integrated lithium niobate microwave photonic processing engine. *Nature* **627**, 80–87 (2024).
33. V. Snigirev, A. Riedhauser, G. Lihachev, M. Churaev, J. Riemensberger, R. N. Wang, A. Siddharth, G. Huang, C. Möhl, Y. Popoff, U. Drechsler, D. Caimi, S. Hönl, J. Liu, P. Seidler, T. J. Kippenberg, Ultrafast tunable lasers using lithium niobate integrated photonics. *Nature* **615**, 411–417 (2023).
34. Q. Guo, B. K. Gutierrez, R. Sekine, R. M. Gray, J. A. Williams, L. Ledezma, L. Costa, A. Roy, S. Zhou, M. Liu, A. Marandi, Ultrafast mode-locked laser in nanophotonic lithium niobate. *Science* **382**, 708–713 (2023).
35. C. J. Sarabalis, R. Van Laer, R. N. Patel, Y. D. Dahmani, W. Jiang, F. M. Mayor, A. H. Safavi-Naeini, Acousto-optic modulation of a wavelength-scale waveguide. *Optica* **8**, 477–483 (2021).
36. L. Shao, M. Yu, S. Maity, N. Sinclair, L. Zheng, C. Chia, A. Shams-Ansari, C. Wang, M. Zhang, K. Lai, M. Lončar, Microwave-to-optical conversion using lithium niobate thin-film acoustic resonators. *Optica* **6**, 1498–1505 (2019).
37. B. Li, Q. Lin, M. Li, Frequency-angular resolving LiDAR using chip-scale acousto-optic beam steering. *Nature* **620**, 316–322 (2023).
38. Y. Yu, X. Sun, Surface acoustic microwave photonic filters on etchless lithium niobate integrated platform. *Laser Photon. Rev.* **18**, 2300385 (2024).
39. J. Bain, M. Mahmoud, L. Cai, M. Khan, G. Piazza, T. Mukherjee, A. Mahmoud, Acousto-optical modulation of thin film lithium niobate waveguide devices. *Photonics Res.* **7**, 1003–1013 (2019).
40. K. Ye, H. Feng, Y. Klaver, A. Keloth, A. Mishra, C. Wang, D. Marpaung, Surface acoustic wave stimulated Brillouin scattering in thin-film lithium niobate waveguides. *arXiv: 2311.14697 [physics.optics]* (2023).
41. C. C. Rodrigues, N. J. Schilder, R. O. Zurita, L. S. Magalhães, A. Shams-Ansari, T. P. M. Alegre, M. Lončar, G. S. Wiederhecker, On-chip backward stimulated Brillouin scattering in lithium niobate waveguides. *CLEO, STH4C.2* (2024).
42. Y.-H. Yang, J.-Q. Wang, Z.-X. Zhu, X.-B. Xu, Q. Zhang, J. Lu, Y. Zeng, C.-H. Dong, L. Sun, G.-C. Guo, C.-L. Zou, Stimulated Brillouin interaction between guided phonons and photons in a lithium niobate waveguide. *Sci China Phys. Mech. Astron.* **67**, 214221 (2024).
43. C. C. Rodrigues, R. O. Zurita, T. P. M. Alegre, G. S. Wiederhecker, Stimulated Brillouin scattering by surface acoustic waves in lithium niobate waveguides. *J. Opt. Soc. Am. B* **40**, D56–D63 (2023).
44. D. Jia, Q. Luo, C. Yang, R. Ma, X. Yu, F. Gao, Q. Yang, F. Bo, G. Zhang, J. Xu, High-efficiency edge couplers enabled by vertically tapering on lithium-niobate photonic chips. *Appl. Phys. Lett.* **123**, 263502 (2023).
45. A. Choudhary, I. Aryanfar, S. Shahnia, B. Morrison, K. Vu, S. Madden, B. Luther-Davies, B. J. Eggleton, D. Marpaung, Tailoring of the Brillouin gain for on-chip widely tunable and reconfigurable broadband microwave photonic filters. *Opt. Lett.* **41**, 436–439 (2016).
46. W. Wei, L. Yi, Y. Jauouën, W. Hu, Bandwidth-tunable narrowband rectangular optical filter based on stimulated Brillouin scattering in optical fiber. *Opt. Express* **22**, 23249–23260 (2014).
47. R. Engelbrecht, Analysis of SBS gain shaping and threshold increase by arbitrary strain distributions. *J. Lightwave Technol.* **32**, 1689–1700 (2014).
48. F. Kong, L. Dong, Precise tailoring of acoustic velocity in optical fibers by hydrogenation and UV exposure. *Opt. Express* **20**, 27810–27819 (2012).
49. M. Zerbib, M. Deroth, T. Sylvestre, K. P. Huy, J.-C. Beugnot, Stimulated Brillouin scattering in silica optical nanofibers. *APL Photonics* **9**, 100805 (2024).
50. Y. Bai, M. Zhang, Q. Shi, S. Ding, Y. Qin, Z. Xie, X. Jiang, M. Xiao, Brillouin-Kerr soliton frequency combs in an optical microresonator. *Phys. Rev. Lett.* **126**, 063901 (2021).
51. M. Nie, J. Musgrave, S.-W. Huang, Cross-polarized stimulated Brillouin scattering empowered photonics. *arXiv: 2405.15888 [physics.optics]* (2024).
52. S. Sun, B. Wang, K. Liu, M. W. Harrington, F. Tabatabaie, R. Liu, J. Wang, S. Hanifi, J. S. Morgan, M. Jahanbozorgi, Z. Yang, S. M. Bowers, P. A. Morton, K. D. Nelson, A. Beling, D. J. Blumenthal, X. Yi, Integrated optical frequency division for microwave and mmWave generation. *Nature* **627**, 540–545 (2024).
53. K. Liu, J. H. Dallyn, G. M. Brodnik, A. Isichenko, M. W. Harrington, N. Chauhan, D. Bose, P. A. Morton, S. B. Papp, R. O. Behunin, D. J. Blumenthal, Photonic circuits for laser stabilization with integrated ultra-high Q and Brillouin laser resonators. *APL Photonics* **7**, 096104 (2022).
54. C. Wei, H. Feng, K. Ye, M. Eijkel, Y. Klaver, Z. Chen, A. Keloth, C. Wang, D. Marpaung, Programmable multifunctional integrated microwave photonic circuit on thin-film lithium niobate. *arXiv: 2409.10227 [physics.optics]* (2024).
55. J. M. S. Domingo, J. Pelayo, F. Villuendas, C. D. Heras, E. Pellejer, Very high resolution optical spectrometry by stimulated Brillouin scattering. *IEEE Photonics Technol. Lett.* **17**, 855–857 (2005).

Acknowledgments

Funding: This work was supported by European Research Council Consolidator Grant 101043229 TRIFFIC (D.M.), European Research Council Proof-of-Concept Grant 101157112

Veritas (D.M.), Nederlandse Organisatie voor Wetenschappelijk Onderzoek (NWO) Start Up 740.018.021 (D.M.), Research Grants Council, University Grants Committee N_CityU11320 (C.Wa.), Research Grants Council, University Grants Committee CityU11204022 (C.Wa.), Research Grants Council, University Grants Committee C1002-22Y (C.Wa.), and Croucher Foundation 9509005 (C.Wa.). **Author contributions:** Conceptualization: K.Y. and D.M. Methodology: K.Y., H.F., D.M., C.Wa., Y.K., and R.t.M. Investigation: K.Y., H.F., R.t.M., C.We., Z.Z., A.M., A.K., Y.K., and Z.C. Visualization: K.Y., H.F., and A.T.I. Funding acquisition: D.M. and C.Wa. Project administration: D.M. and C.Wa. Supervision: D.M. and C.Wa. Writing—original draft: K.Y. and D.M. Writing—review and editing: K.Y., D.M., H.F., C.Wa., Y.K., R.t.M., C.We., A.M., Z.Z., A.K., A.T.I.,

and Z.C. **Competing interests:** The authors declare that they have no competing interests. **Data and materials availability:** All data needed to evaluate the conclusions in the paper are present in the paper and/or the Supplementary Materials and are available at <https://doi.org/10.4121/68ece8a1-8931-4411-bb2a-690d7eadee26>.

Submitted 17 December 2024

Accepted 21 March 2025

Published 30 April 2025

10.1126/sciadv.adv4022